Supporting Information

Electroosmosis-Driven Hydrogel Actuators Using Hydrophobic/Hydrophilic Layer-By-Layer Assembly-Induced Crack Electrodes

Jongkuk Ko[1], Dongjin Kim[2], Yongkwon Song[1], Seokmin Lee[1], Minseong Kwon[1], Seungyong Han[2], Daeshik Kang[2], Yongju Kim[3], June Huh[1], Je-Sung Koh[2*], and Jinhan Cho[1*]

[1]Department of Chemical & Biological Engineering, Korea University, 145 Anam-ro, Seongbuk-gu, Seoul 02841, Republic of Korea

[2]Department of Mechanical Engineering, Ajou University, 206 Worldcup-ro, Yeongtong-gu, Suwon 16499, Republic of Korea

[3]KU-KIST Graduate School of Converging Science & Technology, Korea University, 145 Anam-ro, Seongbuk-gu, Seoul 02841, Republic of Korea

*Address correspondence to jinhan71@korea.ac.kr, and jskoh@ajou.ac.kr.

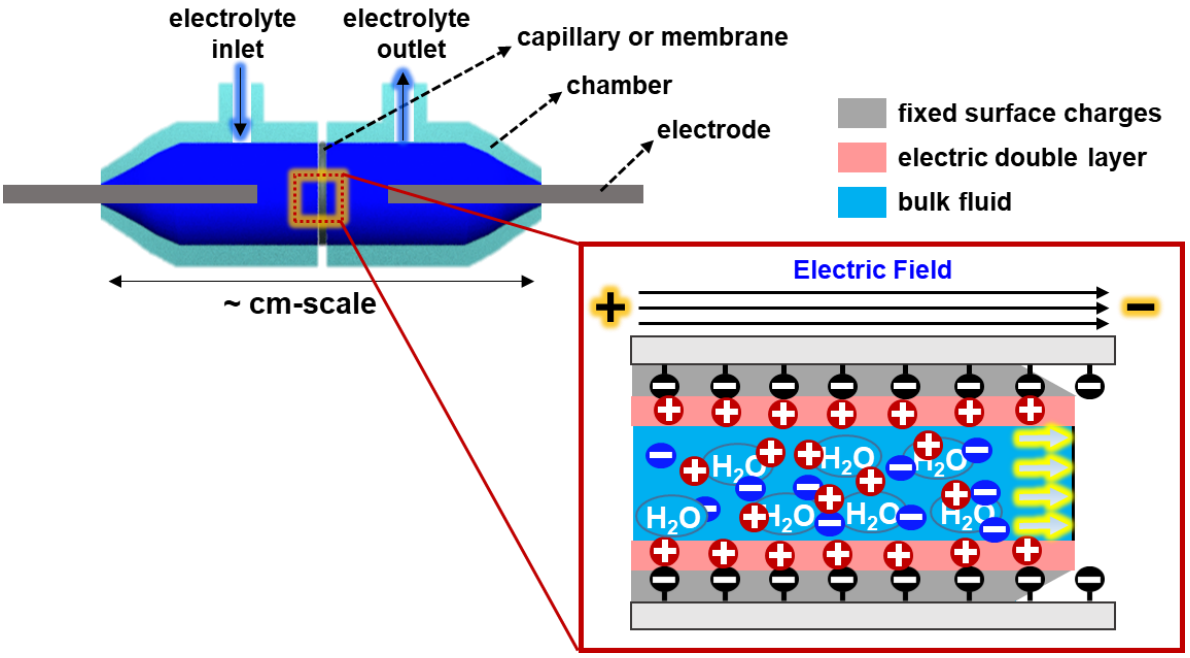

Figure S1. Schematic illustration of typical electroosmosis device with bulky and rigid system. Electroosmosis is the flow of liquid electrolyte in contact with microporous surface of membrane with fixed charges by the applied electric field. When the electrolyte is positioned on the microporous membrane with fixed surface charges, the electric double layers with dominant concentration of counter ions are formed. By applying electric field through microchannel, the ions in the electric double layers move toward an applied electric field, which drags the fluid, and resultantly generate the net movement of bulk fluid.

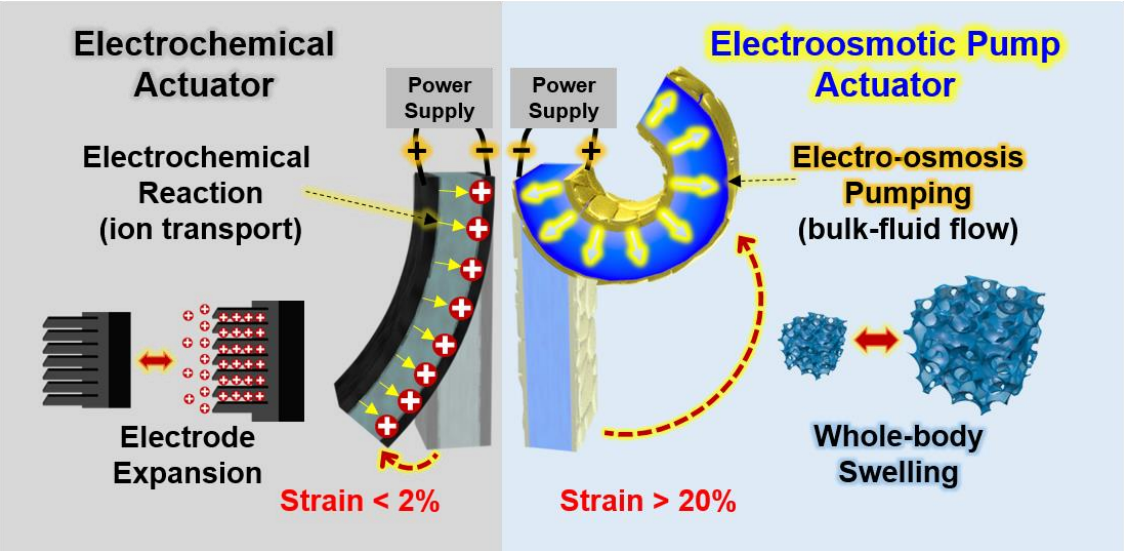

Figure S2. Actuations of electrochemical actuators depend on the expansion of electrode induced by conventional electrochemical reactions such as formation of electric double layers and/or intercalation of ions on electrodes. Therefore, previous studies have been focused on developing higher capacity of electrodes and higher ion mobility of membrane. However, the performance improvement has been restricted due to the limitation of electrochemical reaction-based mechanisms, which mainly occurs on the surface of electrodes, and intrinsic mechanical properties of electrodes.

EOP actuator, in this study, is on basis of the new mechanisms. The net movement of bulk-fluid in hydrogel is generated by electroosmosis, resulting in the swelling of whole-body (hydrogel). Therefore, significantly enhanced actuation strain, energy density and power density could be obtained. In addition, our approach is applicable to various shapes of EOP actuators which enables various operation modes.

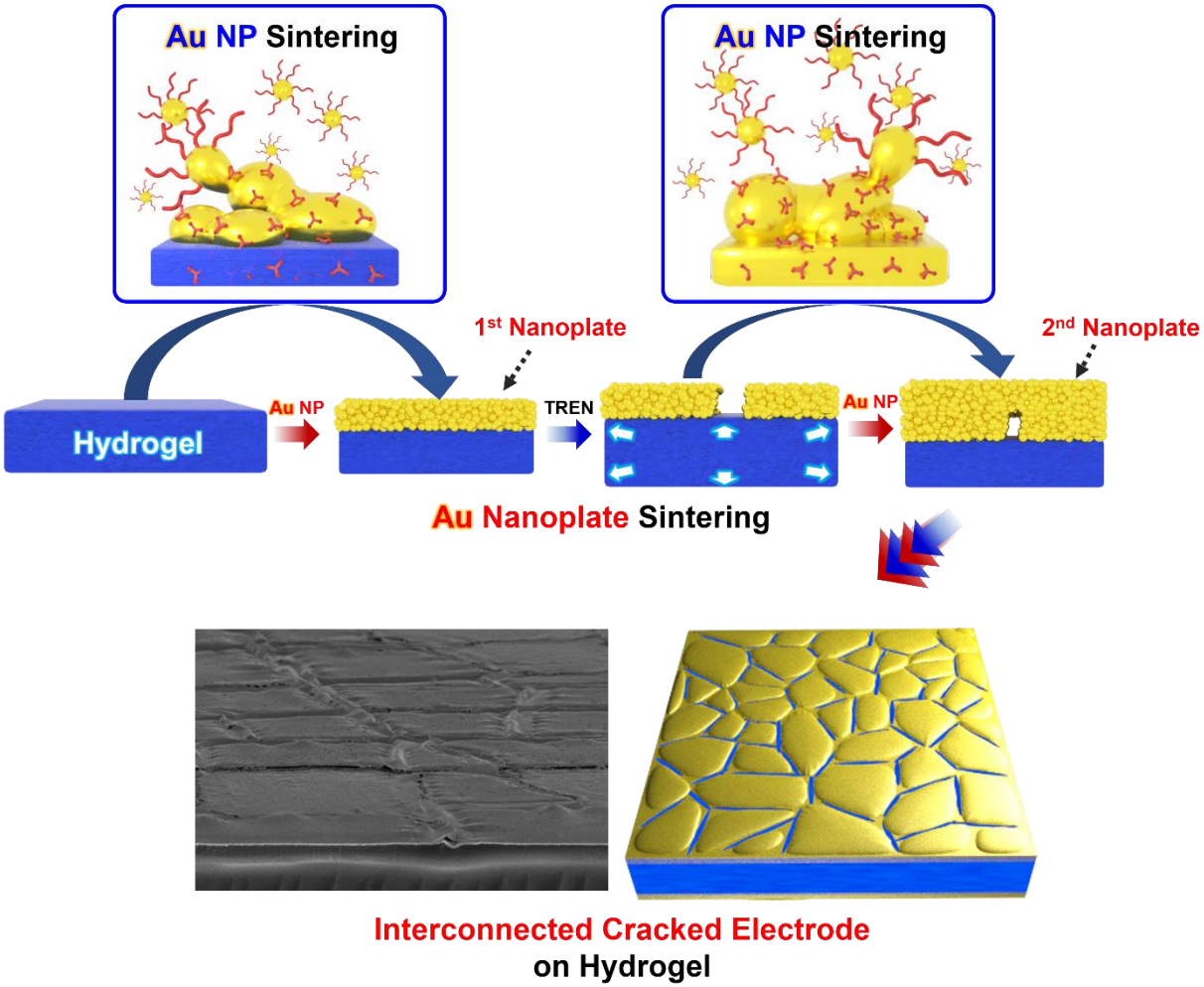

Figure S3. Illustration of interconnected cracked electrodes formed by interfacial assembly and room-temperature sintering of TOA-Au NPs on hydrogels.

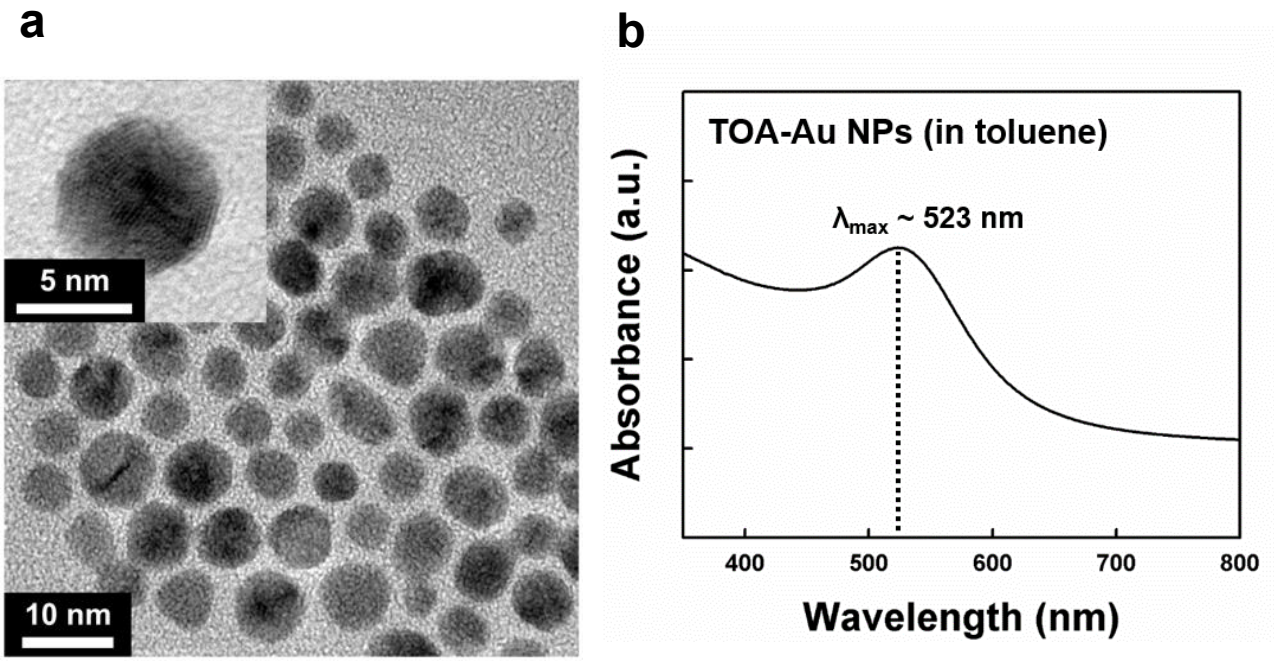

Figure S4. (a) High-resolution TEM image and (b) UV-Vis spectrum of TOA-Au NPs.

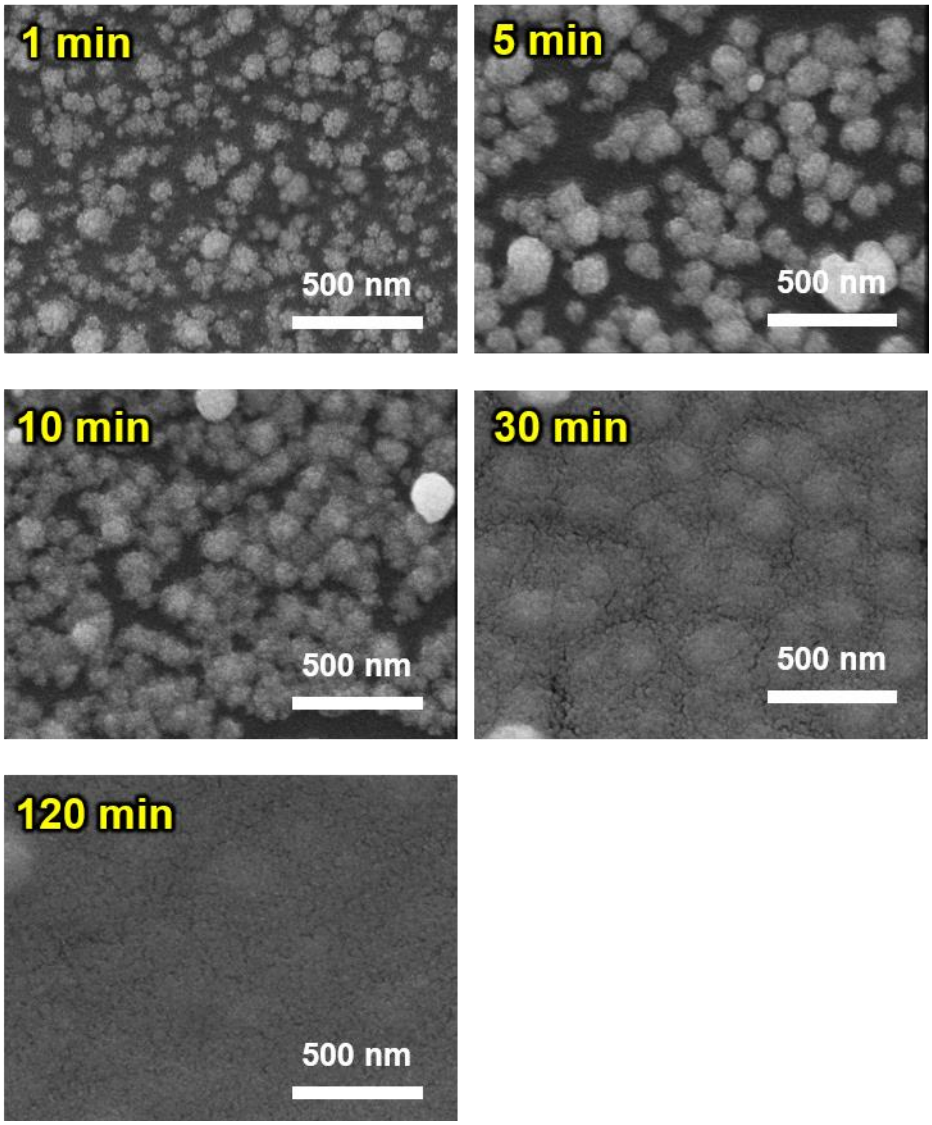

Figure S5. FE-SEM images of room-temperature-sintered Au NPs after adsorption of TOA-Au NPs onto TREN-coated hydrogels for different durations. Poly(acrylic acid)-co-poly(acrylonitrile) (PAA-co-PAN) was used as a hydrogel substrate.

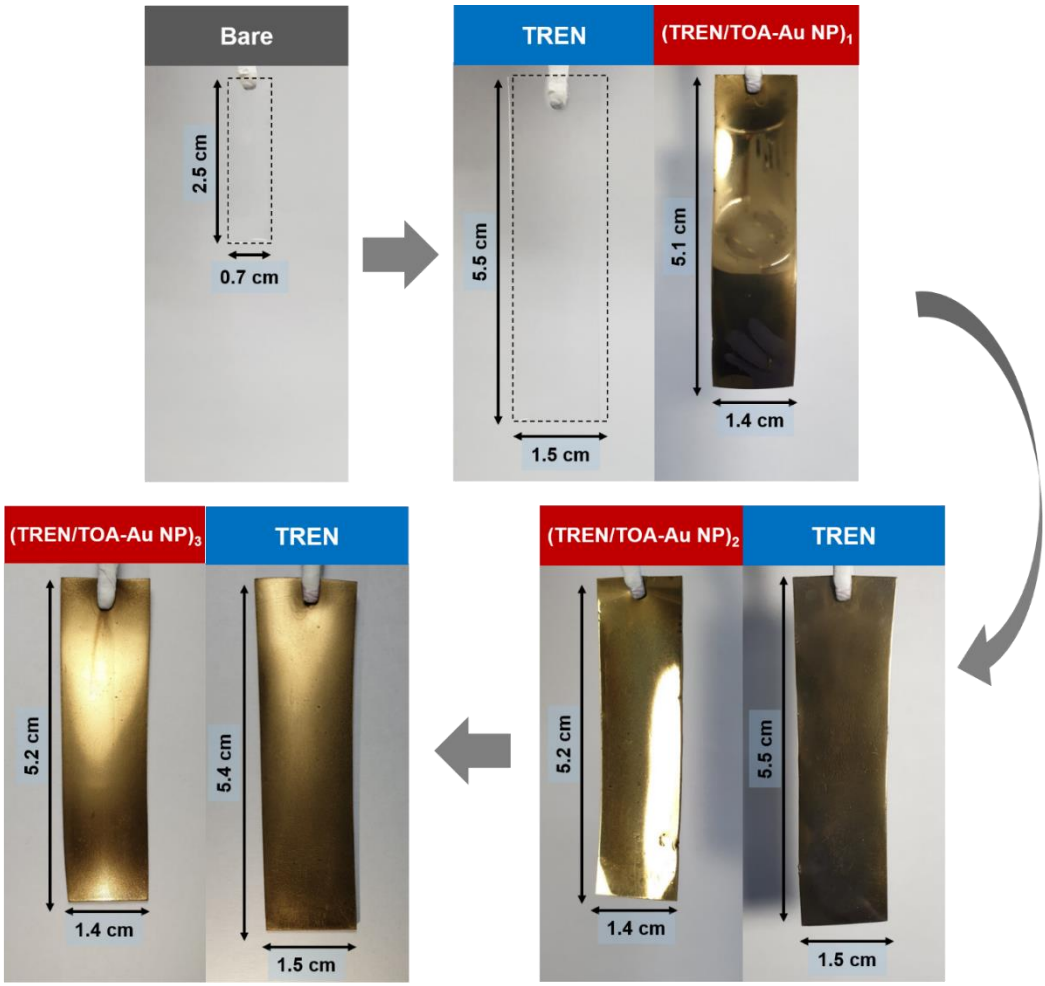

Figure S6. Photographic images of (TREN/TOA-Au NP)$_n$ multilayer-coated PAA-co-PAN hydrogels with different numbers of layers. When the as-synthesized hydrogel was dipped into an aqueous TREN solution (pH 10), the hydrogel significantly swelled up (more than eight times in volume) due to electrostatic repulsion among neighboring carboxylate groups (COO^-) within the hydrogel. Considering that the pK_a (*i.e.*, the pH at which the degree of ionization is 50%) of PAA with a large number of carboxyl groups (COOH) is approximately 4.5, the COOH groups of PAA-based hydrogel are fully deprotonated to COO^- in TREN solution at pH 10[S1,S2]. Therefore, TREN (pK_a ~10) with positively charged amine groups could be electrostatically adsorbed onto negatively charged swollen hydrogels.

The deposition of TOA-Au NPs onto the TREN-coated hydrogels in toluene led to the formation of densely packed and sintered Au NP arrays on the hydrogel surfaces, accompanying contraction of approximately 30% in volume. If the TOA-Au NP-coated hydrogel was dipped into an aqueous TREN aqueous, the hydrogel re-swelled into its initial state, generating the optically undefined surface with numerous micro-sized cracks.

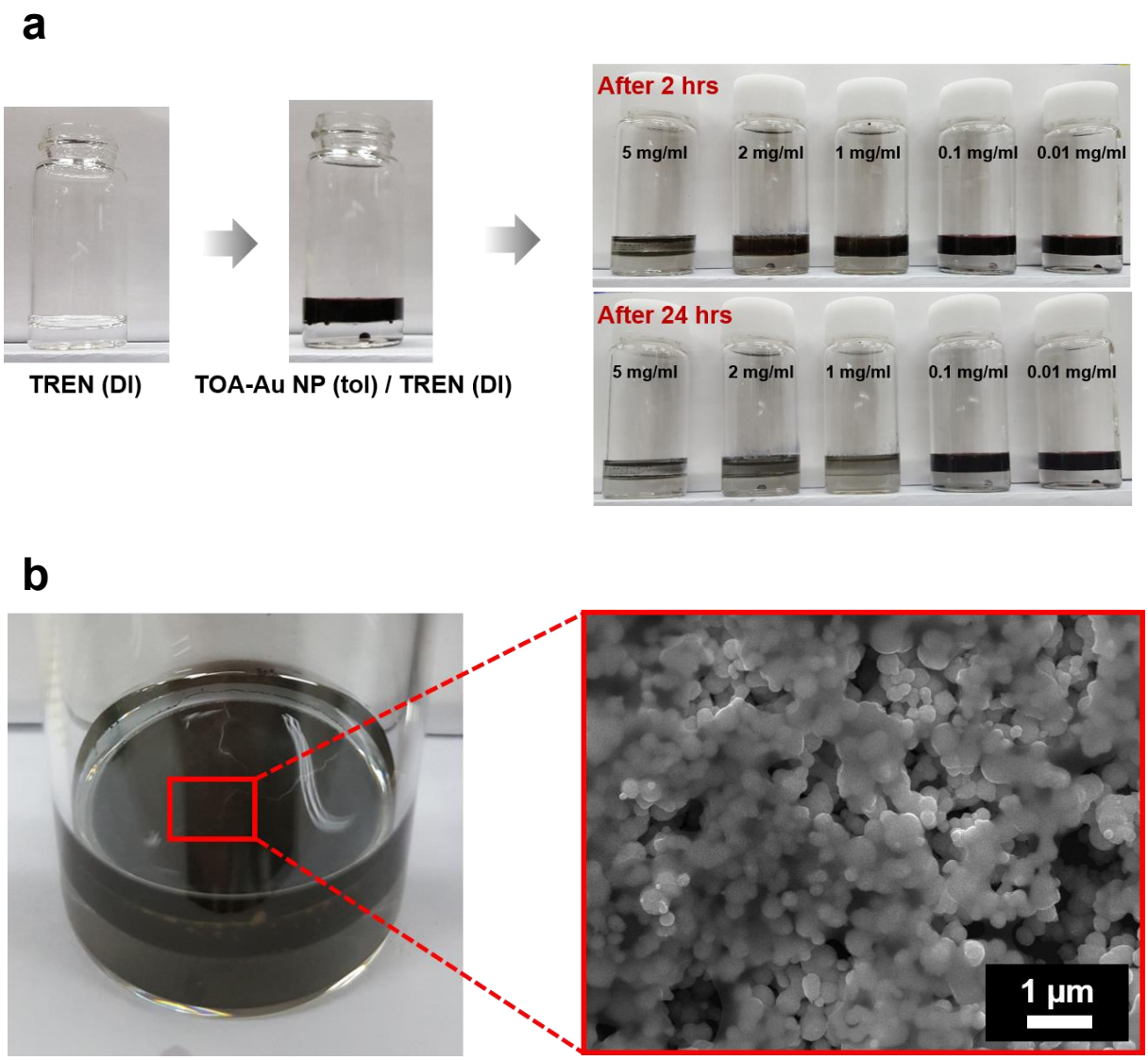

Figure S7. (a) Time- and concentration-dependent interfacial assembly and sintering of Au NPs occurring at the interface between TOA-Au NP (10 mg ml^{-1})-dispersed toluene (tol) and TREN-dissolved water (deionized water, DI) phases. The ligand exchange reaction between TOA and TREN is continuously induced by the higher affinity of TREN for bare Au NPs. Therefore, with increasing TREN concentration in water phases at fixed TOA-Au NP concentrations (10 mg ml^{-1}), the TOA-Au NPs in toluene more rapidly agglomerate at the toluene–water interface. (b) Photographic and FE-SEM images of Au plates formed at the interface between the toluene and water phases. As shown in the FE-SEM image, the sintered Au NPs and the resultant Au nanoplate are formed by interfacial assembly induced by the ligand exchange reaction.

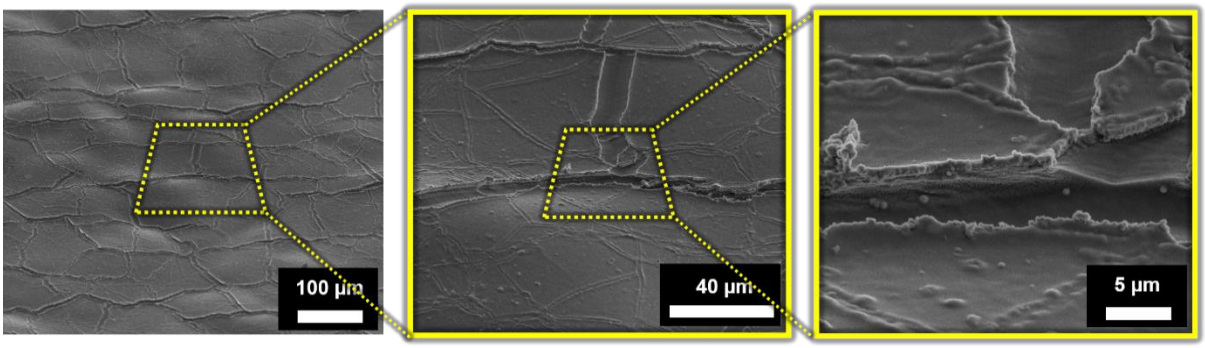

Figure S8. Tilted FE-SEM images of (TREN/TOA-Au NP)$_5$ multilayers coated on PAA-co-PAN hydrogels measured at the same position with different magnification. An interconnected crack structure with crack gaps of a few micrometers was observed. The concentrations of TOA-Au NP and TREN solutions were 10 and 5 mg ml^{-1}, respectively.

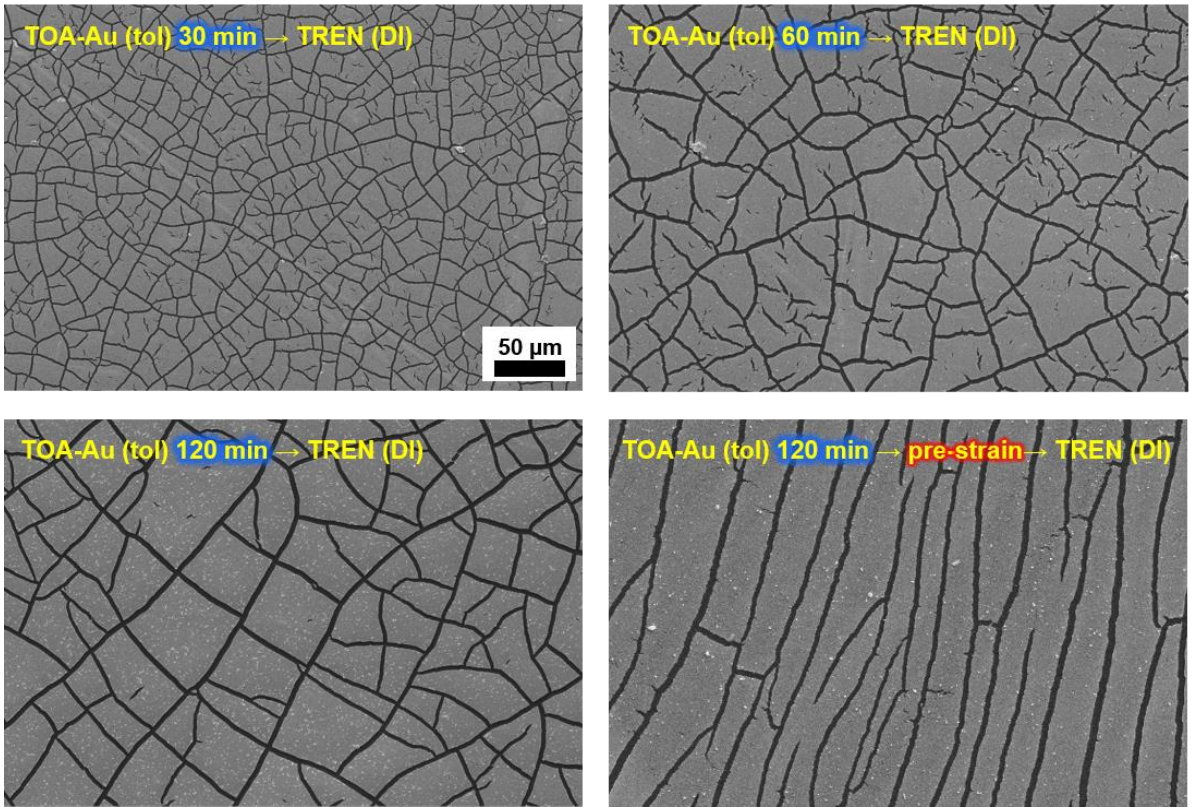

Figure S9. FE-SEM images of TOA-Au NP coated on PAA-co-PAN hydrogels. The sizes of cracks are varied according to immersing time in TOA-Au NP toluene solution. In addition, anisotropic cracks are formed by applying directional pre-strain before the sample was immersed in aqueous TREN solution.

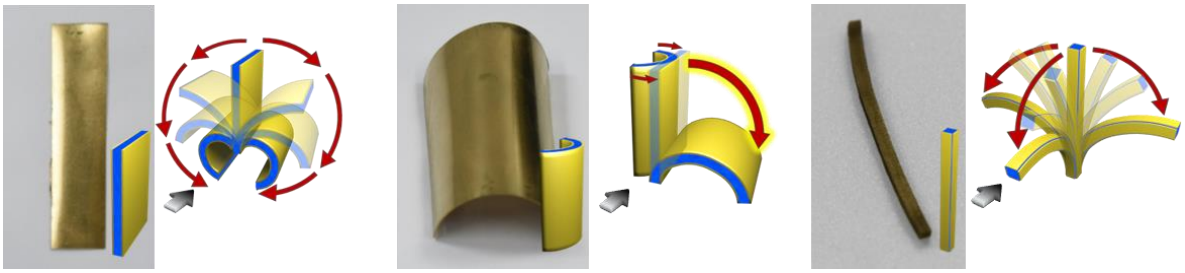

Figure S10. EOP actuators with various shapes for the various operation modes.

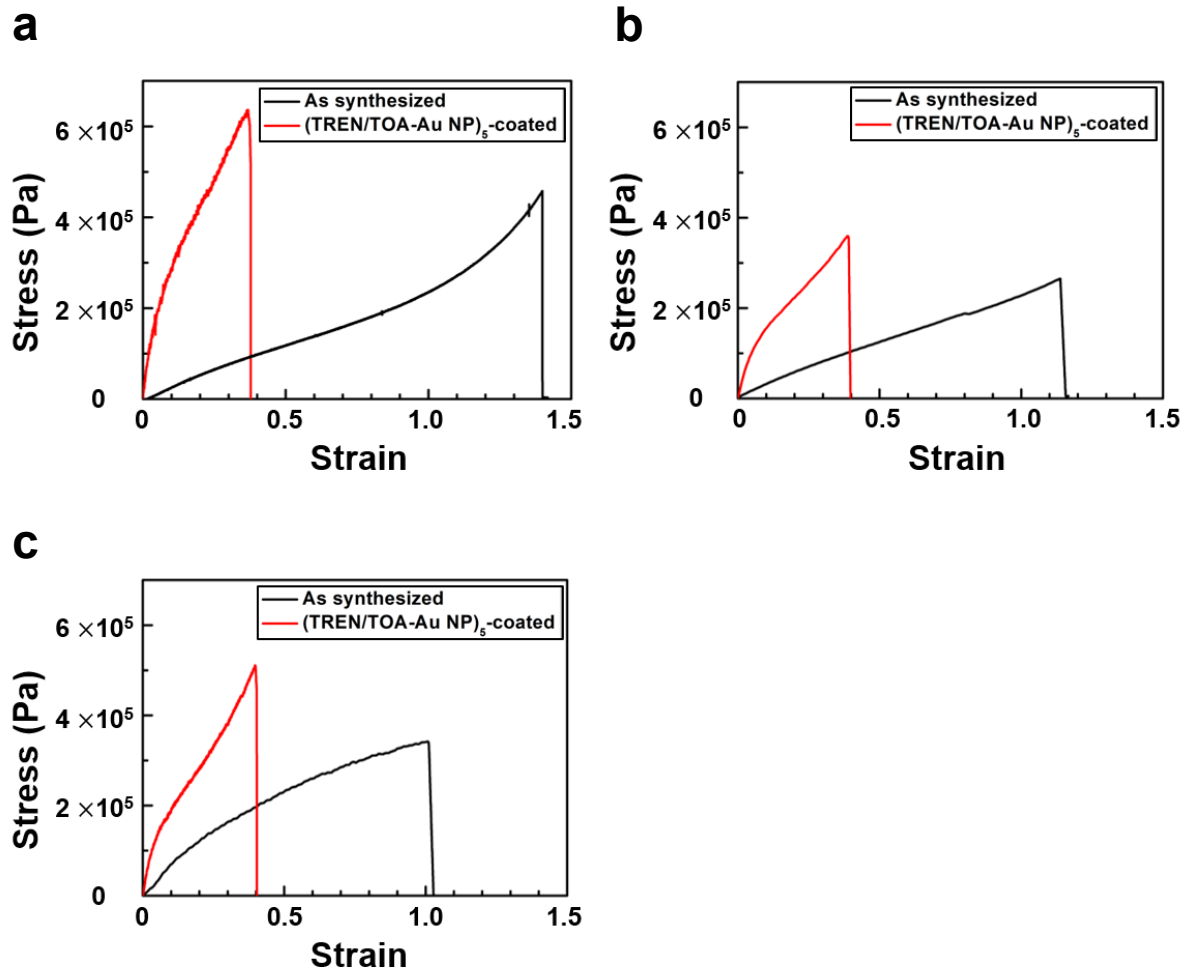

Figure S11. Tensile stress–strain curves of uncoated and (TREN/TOA-Au NP)$_5$-coated hydrogels of (a) PAA-co-PAN, (b) PAA-PVA, and (c) PAA. For the preparation of (TREN/TOA-Au NP)$_5$-coated hydrogels, the concentrations of TOA-Au NP and TREN solutions were fixed at 10 and 5 mg ml^{-1}, respectively.

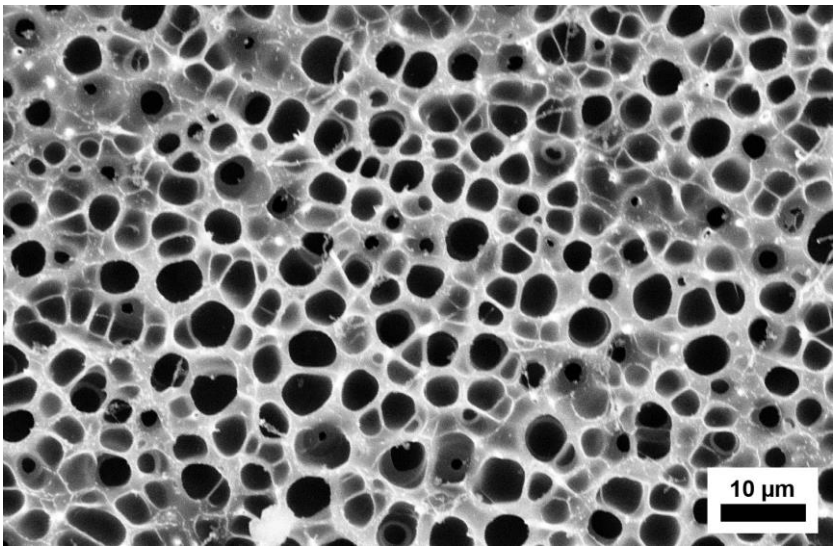

Figure S12. FE-SEM image of freeze-dried poly(acrylic acid)-co-poly(acrylonitrile) (PAA-co-PAN) hydrogel.

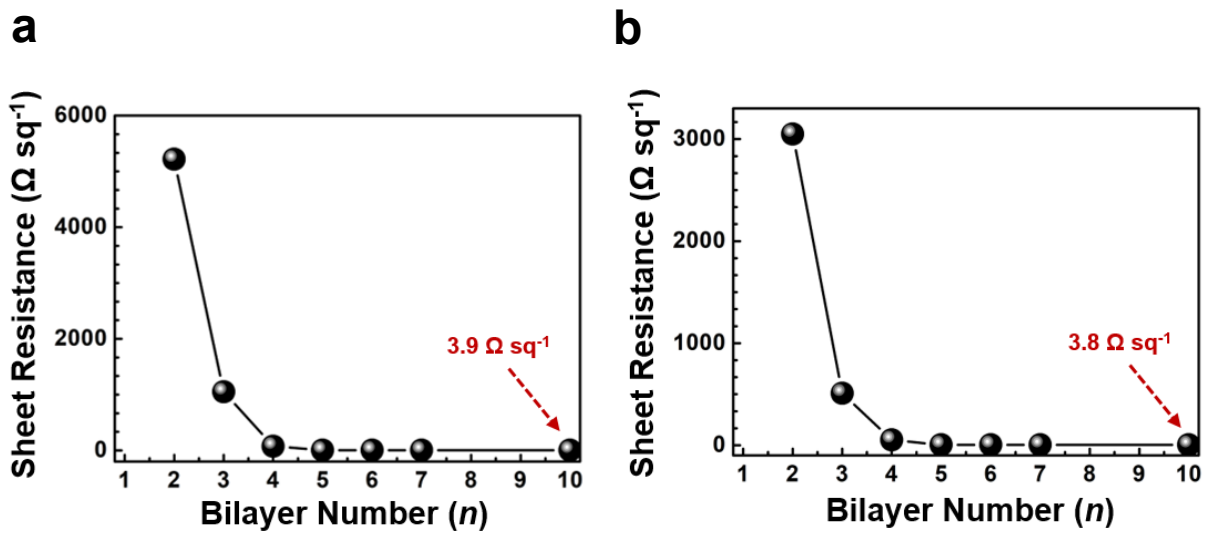

Figure S13. Sheet resistance of (a) $[\text{Au NP}]_n$-coated PAA hydrogel and (b) PAA-PVA hydrogel as a function of bilayer number *n*.

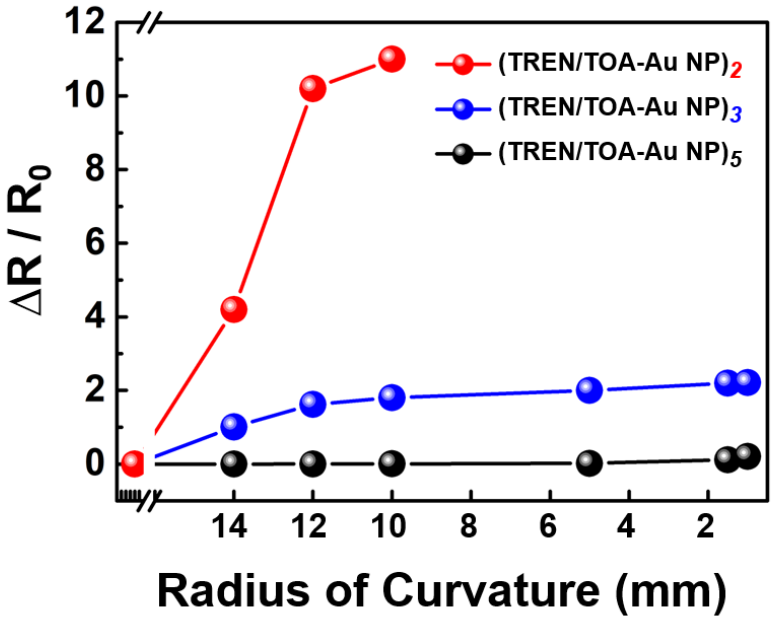

Figure S14. Resistance changes of (TREN/TOA-Au NP)$_n$-coated PAA-co-PAN hydrogel as a function of bilayer number (n) having different number of interconnections.

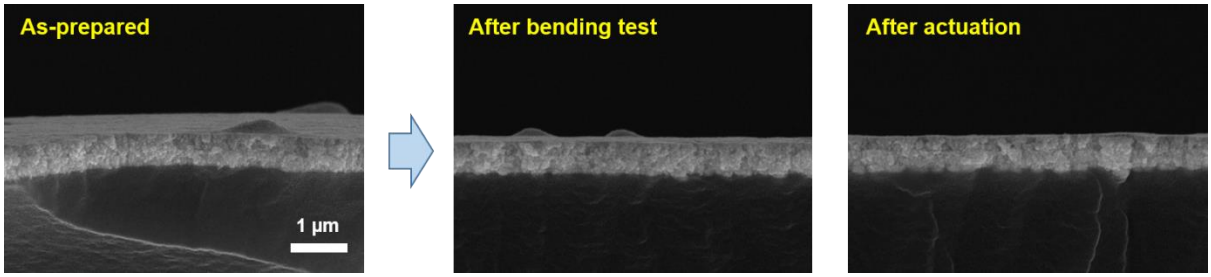

Figure S15. Cross-sectional FE-SEM images of (TREN/TOA-Au NP)$_5$ multilayers coated on PAA-co-PAN hydrogels in the state of as-prepared, after bending cycles of 1,000 times, and after actuation at 3 V.

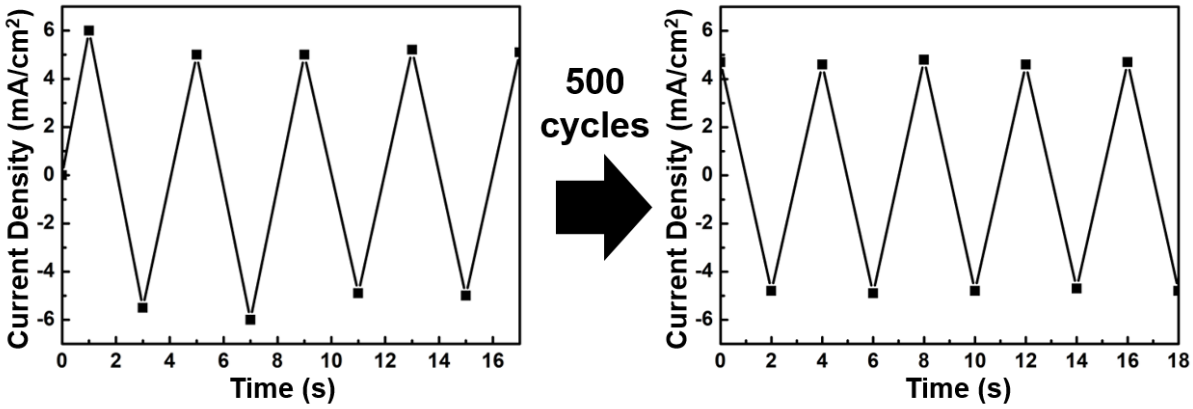

Figure S16. Current density measured on $[Au\ NP]_5$-coated PAA-co-PAN at the applied voltage of ±2 V before and after 500 cycles. Since the electroosmosis flows occur though 1 mm-thick-hydrogels inserted between two cracked electrodes, it is difficult to directly measure the flow rates. Thus, operation stability was approximately estimated by measuring the current density before and after 500 cycles.

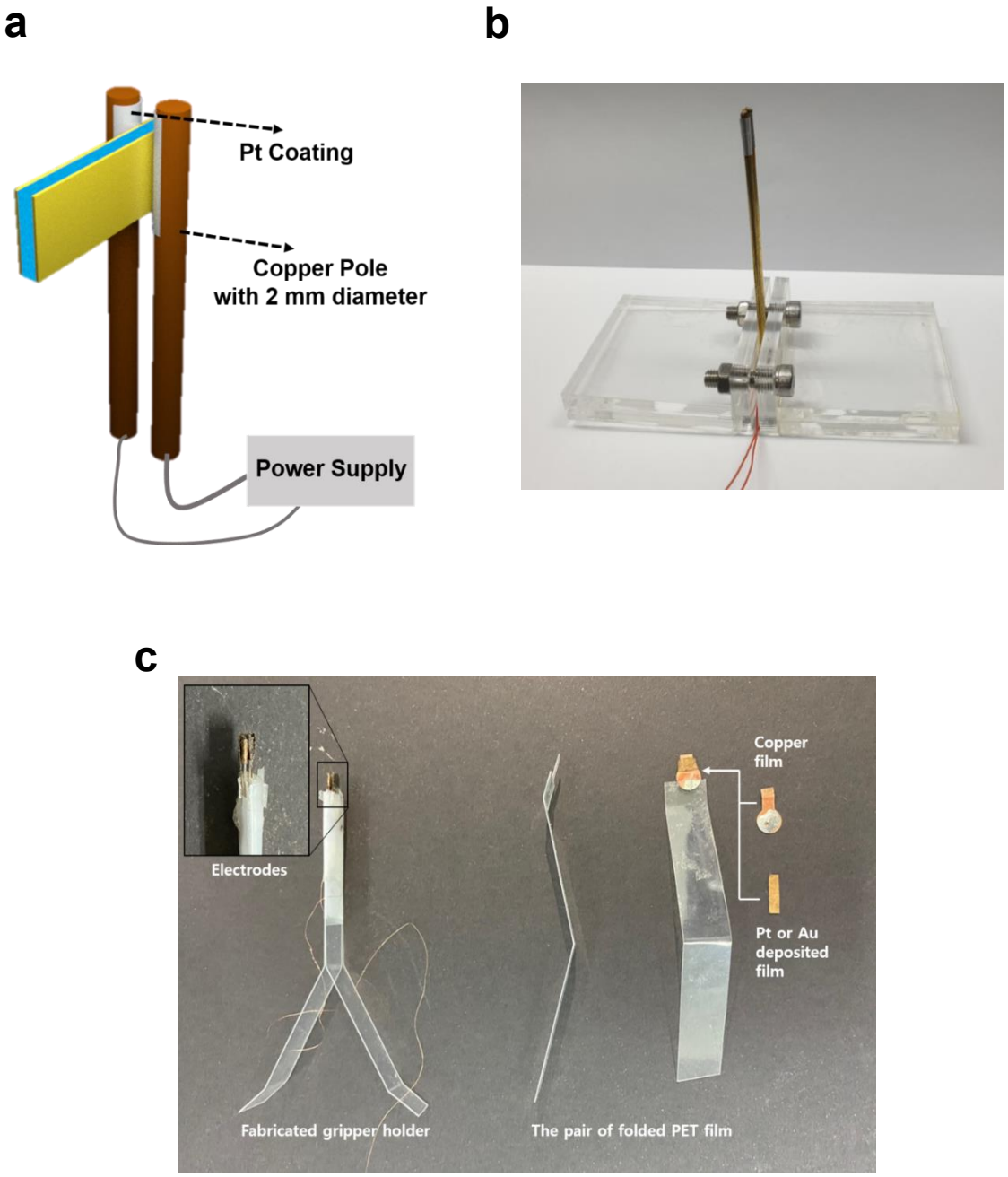

Figure S17. (a) Illustration and (b) photographic images of external support for EOP actuators. (c) Photographic images of external support for soft gripper application. Although plate- or disk-type Pt has typically been used for the actuation of conventional electrochemical actuators, the sharp edges of plain-type Pt can easily damage samples during repeated actuation with a large bending strain. Therefore, in our system, Pt-coated poles with diameters of 2 mm were used to prevent such damage.

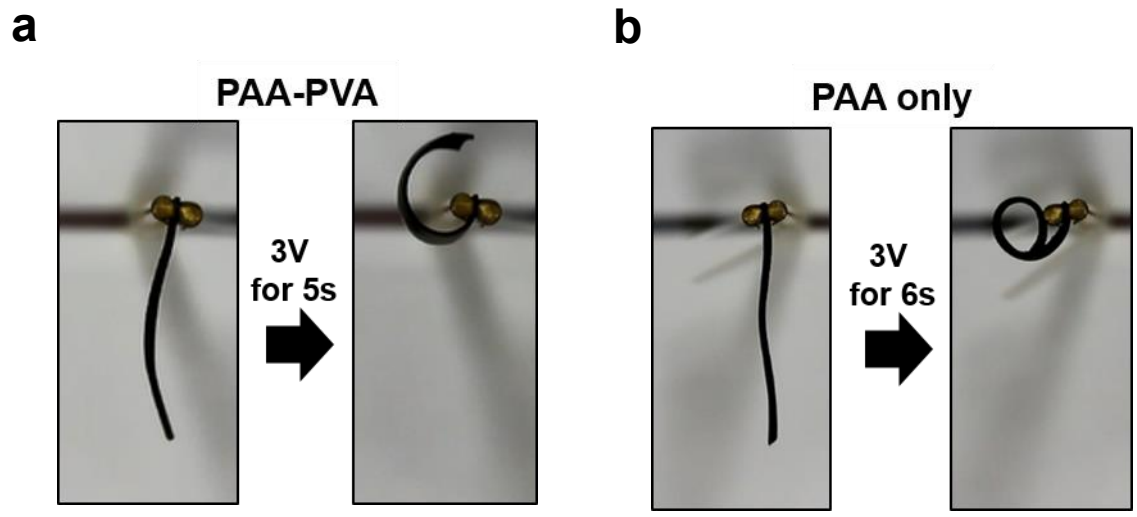

Figure S18. Photographic images of (a) PAA-PVA- and (b) PAA-based EOP actuators operating at 3 V. These results show that hydrogels of different chemical composition as well as PAA-co-PAN-based hydrogels can also be used to prepare EOP actuators with remarkable actuation strains.

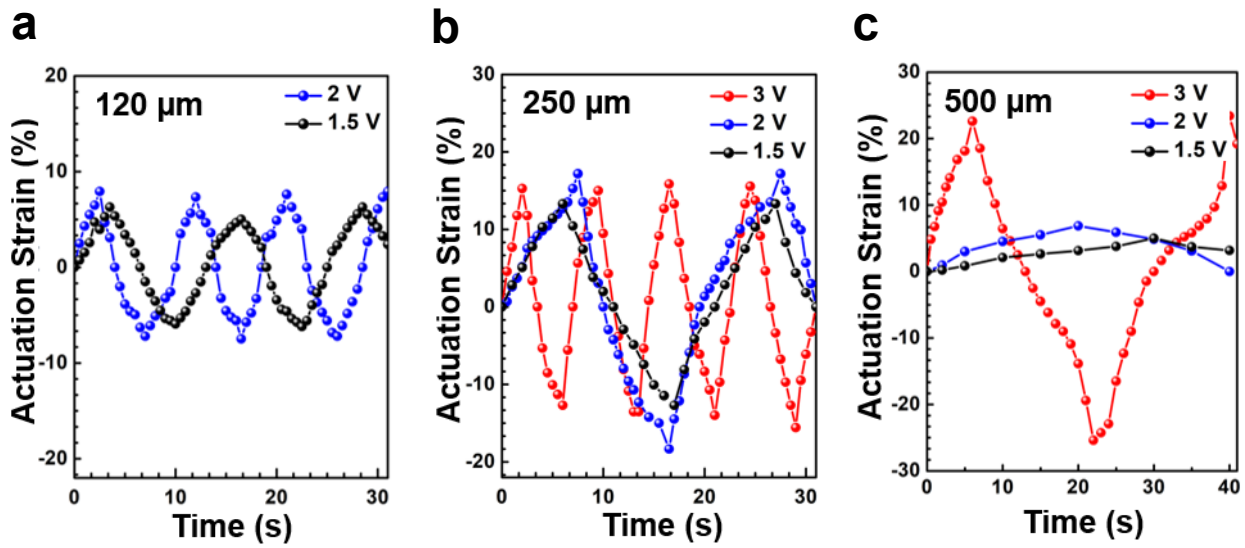

Figure S19. Time-dependent actuation strain of EOP actuators with hydrogel thicknesses of (a) 120 µm, (b) 250 µm, and (c) 500 µm, measured at voltages of 1.5, 2, and 3 V.

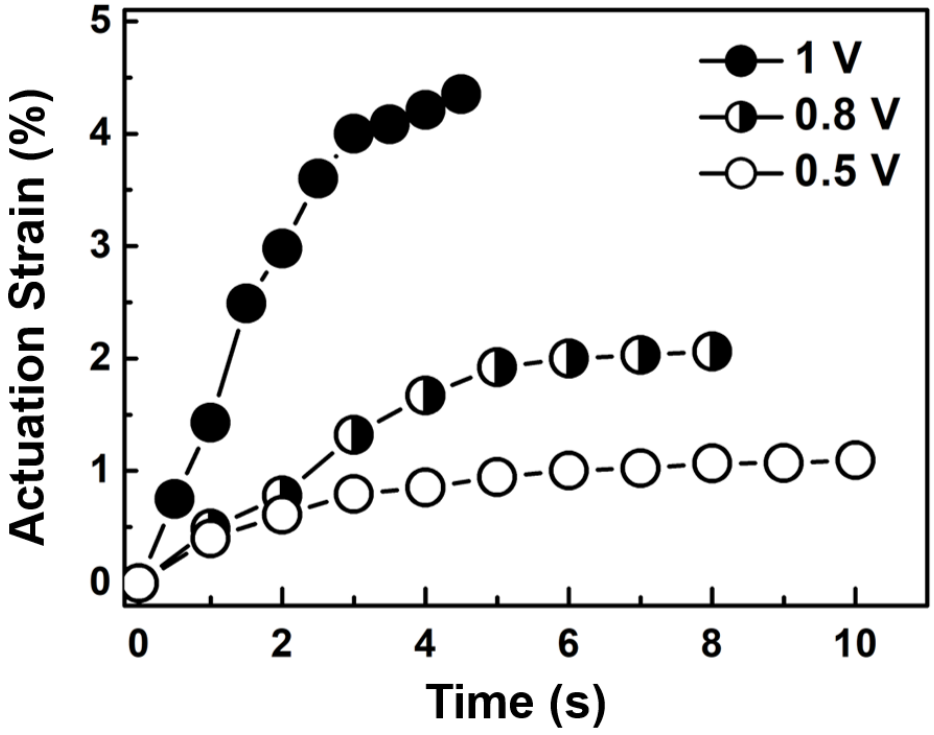

Figure S20. Time-dependent bending strain of a 120-μm-thick EOP actuator operated at voltages of 1, 0.8, and 0.5 V.

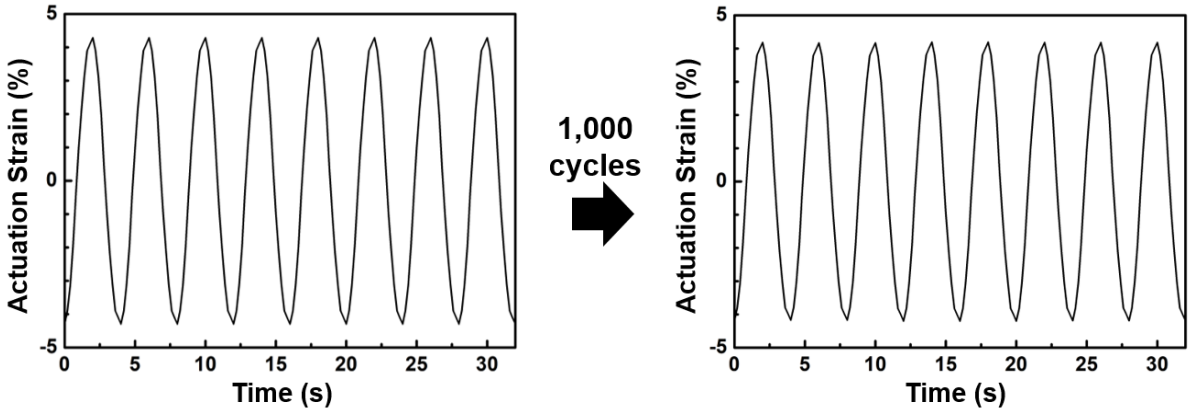

Figure S21. Actuation stability of EOP hydrogel actuators. Samples were soaked in electrolyte solutions for 10 - 20 seconds per every 100 cycles to prevent dehydration by evaporation.

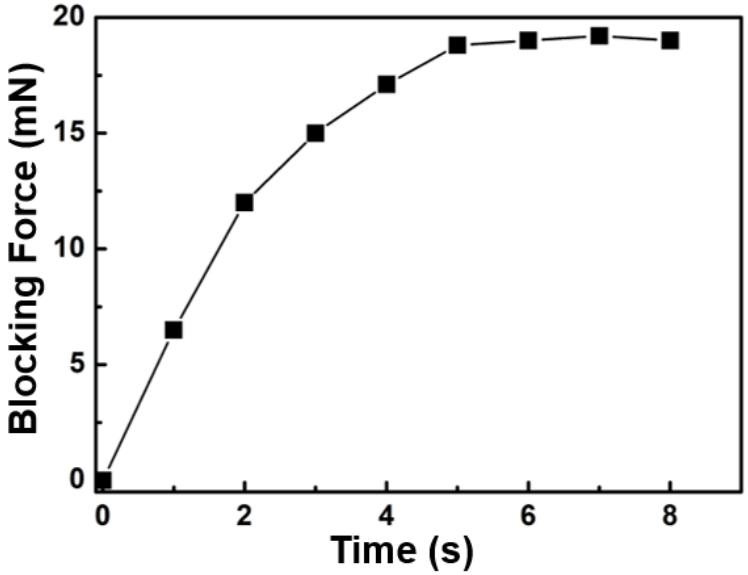

Figure S22. Maximum blocking forces of EOP actuator operated at 3 V as a function of operating time.

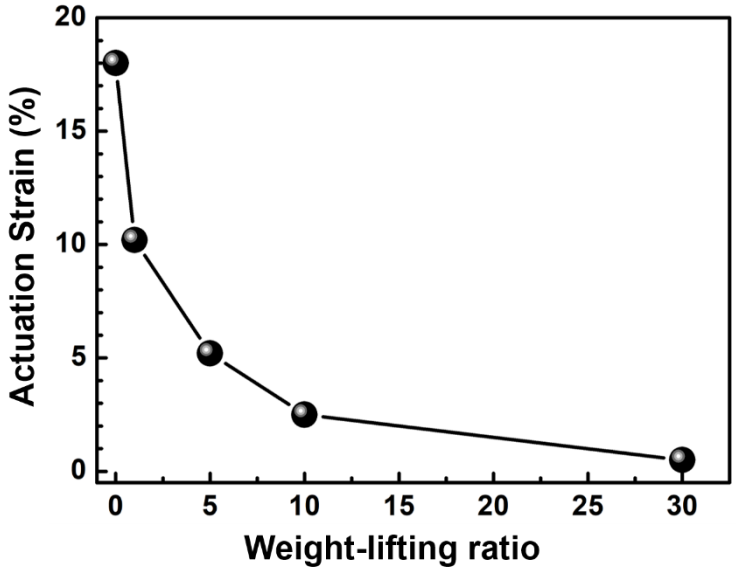

Figure S23. Actuation strain of EOP actuator as a function of weight-lifting ratio under DC voltage of 3 V.

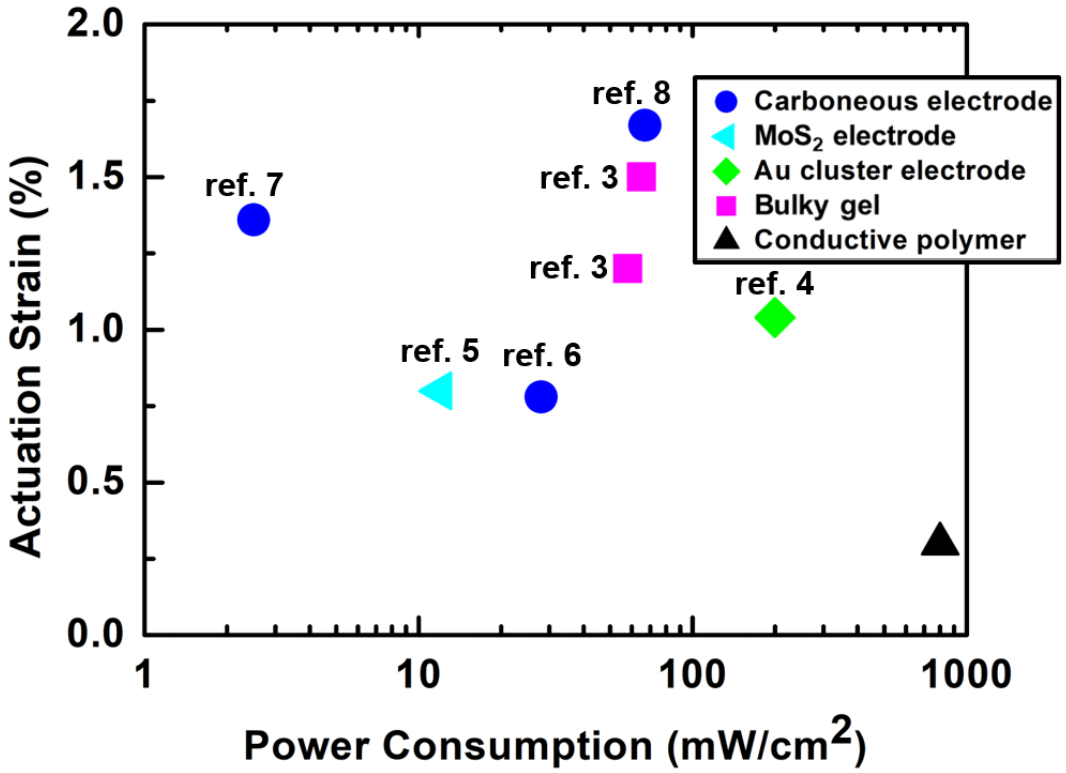

Figure S24. Actuation strain-power consumption dependency of previously reported electrochemical actuators (see **Figure 5a**) are replotted with scaled y-axis. They show actuation strain of less than 2%.

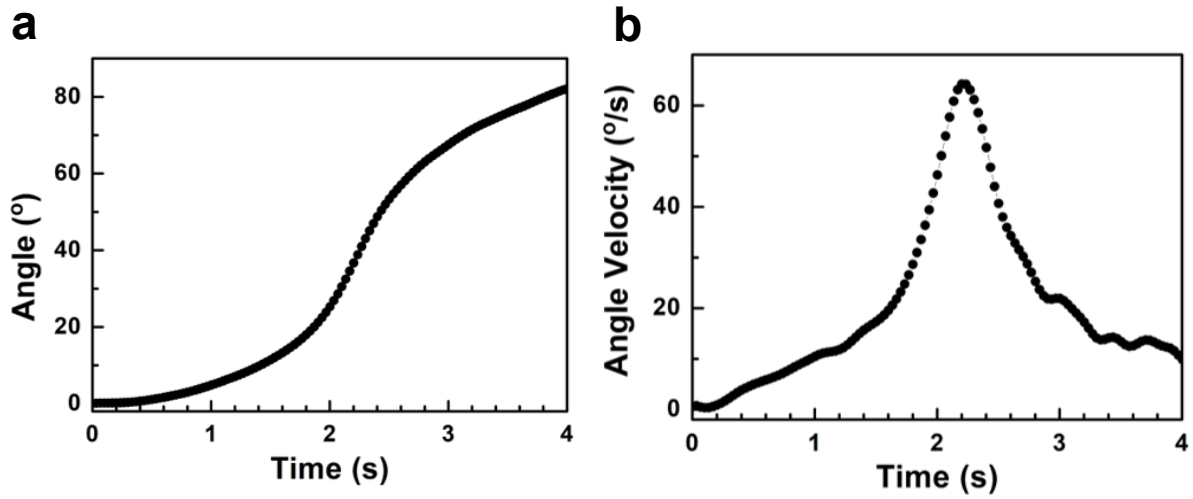

Figure S25. Time-dependent (a) bending angle and (b) angle velocity of a 250-μm-thick EOP actuator with curved-plane shape operated at a voltage of 3 V.

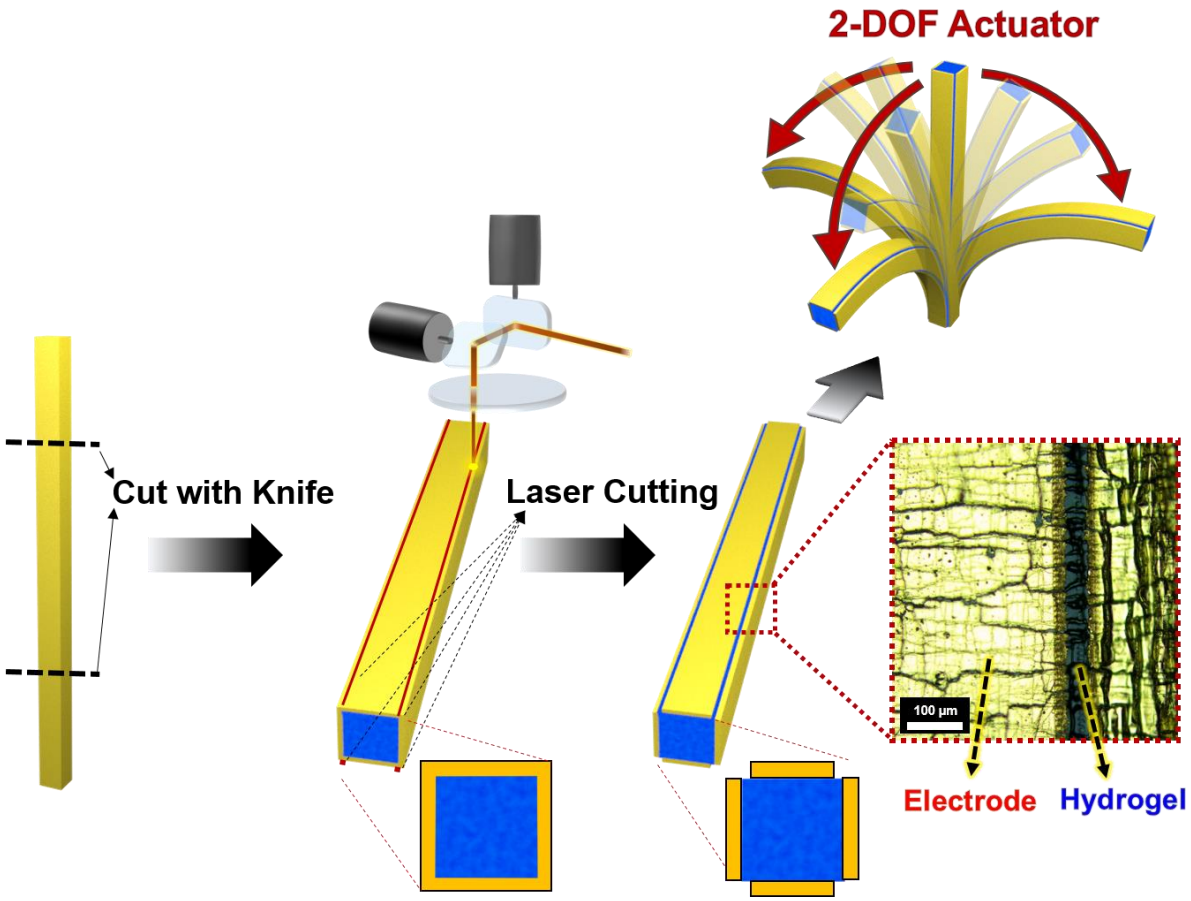

Figure S26. Schematic illustration of the preparation of square-pillared EOP actuator and a photographic image of interconnected cracked electrodes separated by laser cutting. Initially, both ends of the pillared structure-based EOP actuator were cut with a knife. Then, four different sides of the electrodes were separated gaps of 40 μm by laser cutting. Each side of the separated electrodes was connected with external power sources to control the direction of the applied electric field on the EOP actuator.

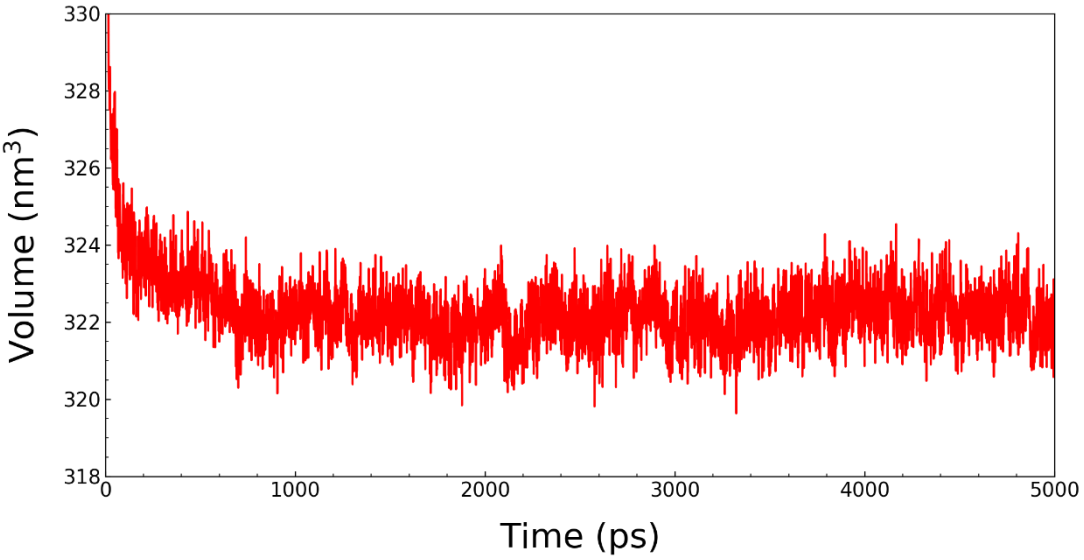

Figure S27. Volume change plotted against the simulation time (for the first 5 ns) for NPT simulation of the present system.

References

[S1] Choi, J.; Rubner, M. F. Influence of the Degree of Ionization on Weak Polyelectrolyte Multilayer Assembly. *Macromolecules* **2005**, *38*, 116–124.

[S2] Cho, J.; Hong, J.; Char, K.; Caruso, F. Nanoporous Block Copolymer Micelle/Micelle Multilayer Films with Dual Optical Properties. *J. Am. Chem. Soc.* **2006**, *128*, 9935–9942.

Movie Captions

Mov. S1. MD Simulation of AuNP sintering. The movie shows 15-ns MD trajectory of the model system consisting of two TOA-Au NPs dispersed in toluene interfaced with water containing TREN. In the movie, AuNP1, AuNP2, TOA, TREN, toluene and water are colored with yellow, light green, red, blue, light red, and light blue, respectively, for visual clarity. It is worth pointing out that the fluctuations of the simulation box in this movie are unnoticeably small, which is partly due to low diffusive Au particles and mainly to isotropic barostat (Berendsen barostat) employed in the present simulation.

Mov. S2. Electroosmosis pumping by interconnected cracked electrode on PAA-co-PAN hydrogel. Ionic liquid is reversibly pumped through the interconnected cracked electrode-coated PAA-co-PAN hydrogel by applying voltage of ± 3 V. The thickness of PAA-co-PAN hydrogel is 1 mm.

Mov. S3. Actuation of EOP actuator with different thickness. Bending motion of EOP actuators (specifically, the $[Au\ NP]_5$-PAA-co-PAN) with thicknesses ranging from 120 to 1300 μm.

Mov. S4. Demonstration of spring-out mode. Reversible spring-out mode of EOP actuator is demonstrated by applying voltage of ± 3 V to the 250-μm-thick EOP actuator. The actuation strain due to the instantaneous release of accumulated energies suddenly increased by 19.3 % for only 0.067 s.

Mov. S5. Soft gripper by planar structure. Stable and efficient operation of EOP actuator as a soft gripper is realized from planar structures. A soft flower with undefined and complex shape as well as battery with heavier weight (1 g) are also grabbed by the EOP actuator.

Mov. S6. Flytrap-like actuation by curved-planar structure. The curved actuator mimicking the structural configuration of *Venus flytrap* exhibits flytrap-like actuation and morphing. The angular velocity is accelerated to 64.2° s^{-1}.

Mov. S7. 2-DOF actuation by square-pillared structure. The bending direction is effectively controlled according to the direction of electric field on four-sides of the square-pillared EOP actuator electrodes.